Vacuum-field Rabi splitting in quantum-well infrared photodetectors

E. Dupont,* H. C. Liu, A. J. SpringThorpe, and W. Lai
Institute for Microstructural Sciences, National Research Council, Ottawa, Ontario K1A 0R6, Canada

M. Extavour
Division of Engineering Science, Bahen Center, 40 St. George Street, University of Toronto, Toronto, Ontario M5S 2E4, Canada

(Received 10 July 2003; revised manuscript received 6 October 2003; published 29 December 2003)

The vacuum-field Rabi splitting due to bound-to-quasibound intersubband transitions in GaAs quantum wells has been demonstrated. A waveguide was designed and the infrared light was resonantly coupled inside with a prismlike technique. Reflection and photocurrent spectra show sharp Rabi doublets. The infrared detectivity of such a structure was investigated with temperature. We have proved that the vacuum-field Rabi splitting of intersubband absorption is easy to observe and has potential applications in optoelectronic devices.

DOI: 10.1103/PhysRevB.68.245320 PACS number(s): 78.66.Fd, 42.50.Hz

I. INTRODUCTION

The observation of a strong coupling between infrared radiation and the intersubband transitions in quantum wells (QW's) has always been challenging, mainly due to the difficulty of generating and manipulating intense infrared coherent waves. With the development of mid-infrared short pulse sources, several groups demonstrated the coherent intersubband polarization[1,2] and the optical free-induction decay in QW's.[3] With more intense sources, partial Rabi flopping could be seen[3] and very recently, complete phase reversal of the intersubband polarization was observed.[4] Semiconductor microcavities, with high quality factors, are also very effective in achieving strong coupling between long-lived photons and excitonic systems. Vacuum-field Rabi splitting in GaAs/AlGaAs microcavities was observed in 1992,[5] and, subsequently, the Bosonic properties of polaritons have been intensively explored.[6–8] In 1997, A. Liu estimated the Rabi splitting of intersubband transitions in an asymmetric Fabry-Pérot microcavity[9] and, earlier this year, an Italian team made the experimental demonstration of the effect.[10] It is to be hoped that, as in excitonic systems, this work will initiate new studies on intersubband transitions in strong-coupling regime. The system of Ref. 10 is based on a waveguide resonator and bound-to-bound transitions. The work reported here is also based on the coupling of intersubband dipoles with a waveguide resonator. In our case, bound-to-quasibound transitions are involved. We show that the exact profile of the Rabi-splitted spectra are complex and not easy to model, even when trying different QW dielectric functions. We demonstrate that intersubband Rabi splitting can be used in optoelectronic devices.

This work was inspired by our earlier experiments on intersubband absorption and photocurrent at grazing internal angles.[11] In Ref. 11 we showed that the absorption profile can be fairly complex at large internal incidence. We also showed that one can excite resonant waveguide modes in standard multiple quantum-well (MQW) structures. Subsequently, we have demonstrated a similar effect in photocurrent spectroscopy.[12] At large internal angles, the contact layers above and below the MQW can act as cladding layers and a slab waveguide is formed. These waveguiding effects cannot be ignored and we proposed to take advantage of them in the design of quantum-well infrared photodetectors (QWIP's) operated at high temperature. The principle consists of exciting a waveguide fundamental mode in close resonance with the intersubband frequency. This would simultaneously lead to high absorption efficiency with a minimal doping level in the wells. Therefore the detectivity at high temperature would be improved.

In this study, the vacuum-field Rabi splitting was easily observable as a result of the reduced dephasing rate of the intersubband coherence in our samples which enhances the peak absorption. The analysis of the spectra gives rise to new questions, such as the possible influence of the continuum states on the Rabi doublet. The paper is organized as follows. In Sec. II, we show results of reflection measurements displaying unambiguous vacuum-field Rabi splitting; in Sec. III we discuss the physics involved and model the observed spectra; in Sec. IV the electrical performances of one of the structures are reported and, finally, we conclude.

II. OPTICAL MEASUREMENTS

A structure, called NT3429, was designed in order to overlap the frequency of the waveguide mode with that of the intersubband resonators at Brewster incidence on the cleaved facet. The designed waveguide uses a combination of dielectric and surface plasmon confinements. This type of waveguide leads to strongly confined TM modes with a reduced epitaxial thickness. Indeed, to observe the same experimental effect without the surface plasmon confinement, the core of the waveguide would have needed to be 43% thicker. The sample was grown by molecular beam epitaxy on a 3-in. (001) GaAs semi-insulating substrate. It consists of a 140-repeat MQW structure embedded between a 0.4-μm-thick n^+ GaAs top contact layer and 0.8-μm n^+ GaAs bottom layer. The Si-doping level in the contacting layers is $2\times10^{18}\mathrm{cm}^{-3}$. The period of the MQW consists of a 60-Å GaAs quantum well and a 290-Å $Al_{0.21}Ga_{0.79}As$ barrier, the center 200 Å of this layer being uniformly doped with Si at a concentration of $10^{16}\,\mathrm{cm}^{-3}$. The equivalent two-dimensional (2D) electron density in the wells is $2\times10^{10}\mathrm{cm}^{-2}$. Practically, the structure is nothing but a stan-

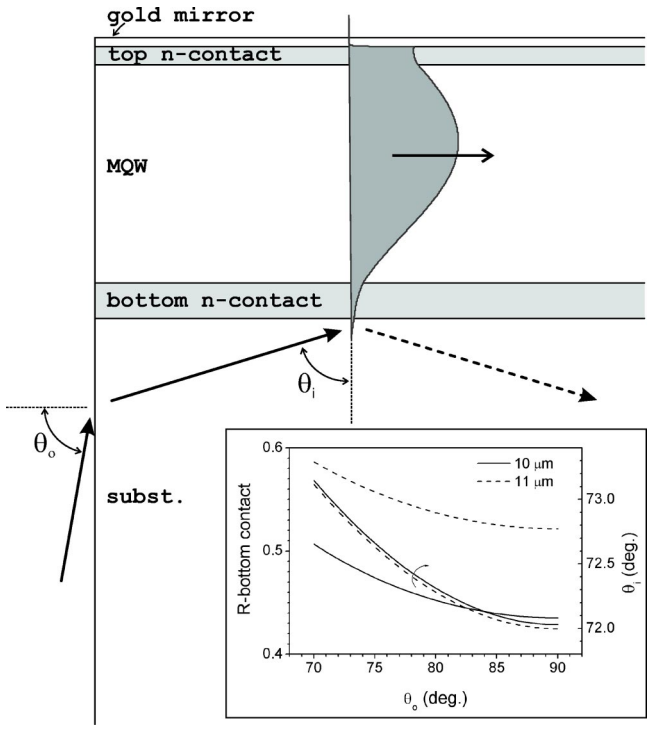

FIG. 1. Schematic of the prismlike coupling technique to couple the infrared light into the QWIP waveguide. The inset plot shows the reflectivity of *P*-polarized light of the 8000-Å n^+ GaAs bottom layer for two wavelengths, 10 and 11 μm. The right scale of the inset plot shows the relation between the external incident angle on the facet θ_o and the internal incident angle θ_i.

dard QWIP structure designed for a wavelength detection at 11–10 μm, the only differences being the small doping level ($\sim$20 times lower than what is used for thermal imaging) and the number of repeats ($\sim$3 times more wells than in thermal imaging). The x-ray-diffraction rocking curve recorded with a $\pm$3.6 arc sec resolution suggests that the quantum well thickness is 60.1 Å, the barrier 286 Å, and the Al content of the barrier 0.197 ± 0.01. Secondary-ion mass spectroscopy (SMIS) indicates, within the accuracy and sensitivity of the technique, that the actual Si concentrations in the structure are close to the nominal values.

Figure 1 is a schematic of the coupling technique used in most of the experiments reported in this paper. *P*-polarized infrared light is directed onto the cleaved facet, refracted inside the substrate and, if the in-plane wave vector of the radiation matches the effective wave vector of the waveguide mode, the light is efficiently coupled inside the slab waveguide. This results in the reflection from the MQW being attenuated. Changing the internal incident angle θ_i by $\Delta\theta_i$ will shift the resonant wavelength of the resonator λ_o by $\Delta\lambda_o$ according to

$$-\frac{\Delta\lambda_o}{\lambda_o} \approx \frac{\sin\theta_i \cos\theta_i}{\left(\frac{n_c}{n_s}\right)^2 - (\sin\theta_i)^2} \Delta\theta_i, \qquad (1)$$

where n_c and n_s are the indices of refraction in the MQW and the substrate. This equation is derived from the phase

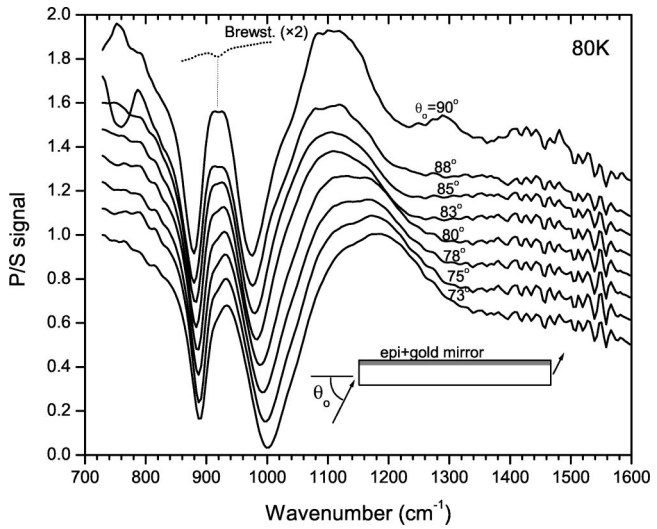

FIG. 2. Normalized ratios between *P*-polarized and *S*-polarized transmittance of the waveguide sample for different incidence on the cleaved facet. The spectra are normalized to unity at around 700 cm^{-1} and, for clarity, the spectra are shifted relative to each other by 0.12. The dashed curve is the *P*-polarized transmittance of the wafer near Brewster incidence (70°) on the plane of the layers.

condition describing the constructive interference of parallel rays inside a waveguide. The contribution from the phase shift on reflection is neglected in this equation. From $\theta_o = 70°$ to $\theta_o = 90°$ the resonant frequency will be lowered by about 100 cm^{-1}. The waveguide is designed to be partially leaking into the substrate with the help of the thin bottom contact layer. The reflectivity of the bottom mirror, $R1$, is wavelength dependent due to the free-carrier absorption (inset of Fig. 1). Therefore a reduced internal incident angle θ_i will redshift the resonance and, as a result of a higher reflectivity of the bottom mirror at longer wavelength, the quality factor (Q factor) of this prismlike waveguide resonator will increase. Q is calculated to be 11 at 73° incidence and 14 at 90°.

The transmission spectrum of the wafer was measured at 80 K, with *P*-polarized infrared light at Brewster incidence (70°) on the plane of the layers. For the reference sample of this absorption measurement, we first took a piece from the same wafer with the epilayers removed and we measured the transmission for *P*-polarized light; then we repeated the same measurement with the epilayers on the substrate. With this measurement at Brewster we avoid the effect of the waveguide and we can get the exact resonance frequency of the intersubband transition. The resolution of all the spectra presented here is 8 cm^{-1}. In Fig. 2 (dashed curve) we identify a small dip of $\sim$1.5% at 920 cm^{-1}. The magnitude of absorption is consistent with bound-to-quasibound transitions. The full-width at half maximum (FWHM) of the peak is $\sim$18 cm^{-1}. This FWHM is small for such thick structure and for bound-to-quasibound transitions. According to simulations, this FWHM of 2.2 meV could be limited by the tunneling of the first excited state to the adjacent wells. If this small intersubband broadening is limited by tunnelling, it implies that other mechanisms of scattering such as optical-phonon emission and interface roughness are not

very effective. Scattering by interface roughness is significant for thin (below 100 Å) quantum wells.[13,14] For this bound-to-quasibound transition where the exact eigenenergy and wave function of the excited state are uncertain, the lower limit for the optical-phonon scattering time would be $\tau \sim 1$ ps. Therefore this scattering mechanism would contribute, at most, for $\hbar/\tau = 0.6$ meV of the line broadening. More sophisticated experiments would be required to distinguish between the different sources of intersubband line broadening. New wafers with bound-to-bound transitions will be tested soon.

A 25/2000 Å Ti/Au mirror was deposited on the epilayers and the sample was cleaved to a length of $2 \times n \times d$, where n is the index of refraction of GaAs at 11 μm, and d the thickness of the sample. With this parallelogram, the light bounces once on the epilayers and maximum throughput is insured. The sample was mounted inside a liquid-nitrogen dewar, which was mounted on a rotating stage. Transmission of *P*- and *S*-polarized light through the parallelogram was measured with a Fourier transform infrared spectrometer. The focusing optics has an aperture of $f/10$, meaning that the angular distribution would have a $1/e$ width of $\pm 6.3°$. Our measurements are therefore convoluted by a Gaussian distribution of angles. The set of spectra of Fig. 2 shows the ratio between *P* and *S* polarizations. At ~ 700 cm^{-1}, i.e., in a spectral region far from the waveguide and intersubband resonances, the QWIP structure is very reflective. The ratio P/S at 700 cm^{-1} should then be calculable by Fresnel laws. We have checked that this ratio is close to the predicted values, confirming that the incident angles are correct within $\pm 1.5°$. In Fig. 2 we have plotted the spectra normalized at 734 cm^{-1} and vertically shifted for clarity. Very intense negative peaks in the QWIP reflection are observed. The upper branch, at 980–1000 cm^{-1}, is narrower as the incident angle is closer to 90°. Even though not very visible on this plot, the opposite phenomenon is happening at the lower branch (880–890 cm^{-1}), i.e., the FWHM of this peak increases with the incident angle. At 90°, the FWHM of both peaks are comparable, indicating that the anticrossing is almost reached. Close to Brewster incidence on the cleaved facet, we see on the high-energy side of the lower branch a shoulder whose position matches exactly the intersubband resonance (920 cm^{-1}). At 90° the intersubband resonance appears as a tiny dip in between the two branches. A positive peak ranging from 1100 to 1200 cm^{-1} depending on the angle of incidence dominates the high-energy side of the upper branch. This peak is the signature of a weakly confined TE mode.

The structure NT3429 was studied in detail optically and electrically. However, exact anticrossing was not reached with this structure. Therefore four more wafers NT3554, 3555, 3556, 3557 with different thickness have been grown. They were similar to the first structure NT3429, except for the nominal Al content in the barrier (22%) and the number of repeats. They contained 130, 140, 150, and 140 repeats, respectively, in order to change the thickness of the waveguide, and therefore to tune the relative position of the waveguide resonance with respect to the intersubband resonance. The wafer NT3557 is a repeat of NT3555 within the run-to-run fluctuations of the growth. From x-ray-diffraction measurements, the derived quantum well thickness are respectively 63.2, 64.3, 63.9, 59.1 Å, the barrier thickness: 298.5, 302, 300.5, 292 Å, and the Al content in the barrier 0.193, 0.197, 0.20, 0.236 ± 0.01. Taking the optical thickness (at 920 cm^{-1}) of the MQW of NT3555 as unity, the optical thickness for NT3554, 3556, and 3557 are respectively 0.9178, 1.0650, and 0.9533. The same reflection experiment at grazing internal incidence has been carried out with these wafers. Results are summarized in Fig. 3.

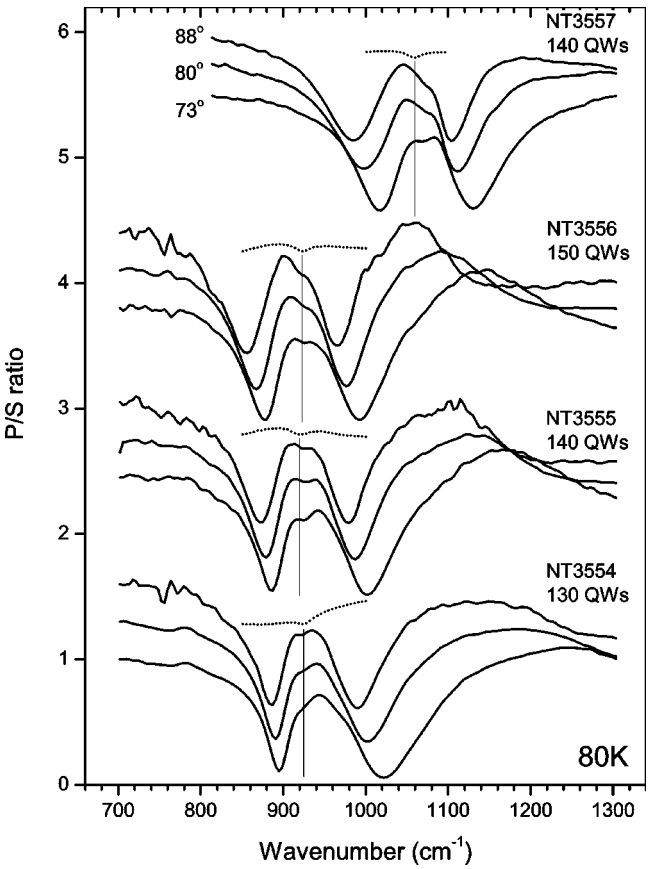

FIG. 3. Ratios P/S (solid lines) of four waveguide structures. The dashed lines represent the *P*-polarized transmittance of the wafers near Brewster incidence (70°) on the plane of the layers. Spectra at 73, 80, and 88° incidence on the cleaved facet are plotted for the four samples.

As the incidence is increased on the facet of NT3554, the upper branch is redshifted and its FWHM decreases. Overall, the lower branch is closer to the intersubband resonance than the upper branch: the waveguide cavity is positively detuned with respect to the intersubband resonance. For NT3555, the anticrossing happens at 90° incidence. For this incidence the FWHM of the two peaks are similar (~ 52 cm^{-1}). We define the occurrence of anticrossing when the two branches are equally spaced from the intersubband resonance. The thickest sample NT3556 shows an anticrossing at $\sim 78°$. At this angle the FWHM of both peaks is also ~ 52 cm^{-1}. This value matches the theoretical value of half the sum of the FWHM of the intersubband and waveguide resonances.[15] At large incidence (88°) the upper branch has a slightly smaller

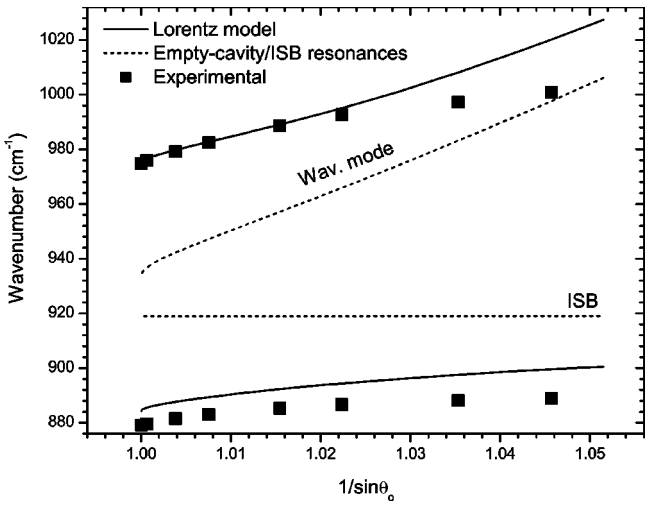

FIG. 4. Wave number of the upper and lower branches of the vacuum-field Rabi effect versus the inverse of the sine of the external angle θ_o. The dashed lines represent the position of the intersubband oscillator (as measured) and waveguide resonator (as calculated). The solid lines are the theoretical peak positions of the Rabi splitting using a Lorentzian model for the imaginary part of the QW dielectric function. The squares represent the positions of the upper and lower branches in Fig. 2.

FWHM than the lower branch. On wafer NT3557 the anticrossing occurs also at $\sim 78°$. Beyond this angle (negative detuning) one can observe a rapid change of the FWHM of the two branches due to the large difference of dephasing rate of the two resonators. Again, for these fours wafers, between the two polaritons branches, more precisely at the intersubband resonance of the QW's, we observe a dip or a shoulder in the reflection spectra. Having demonstrated the anticrossing, the rest of the paper focuses on the first sample (NT3429).

III. MODELING THE REFLECTION SPECTRA

The experimental peak positions versus $1/\sin\theta_o$ are compared with simulations in Fig. 4. The agreement is reasonable but not perfect. For this simulation we adopted a Lorentzian model for the dielectric function ε_{zz} of the QW and we fixed the oscillator strength to unity.[16] The calculation is based on the transfer-matrix method in anisotropic materials and it uses the effective-medium approach.[17] The mobility of the contacting n^+ layers was set at 3000 $\mathrm{cm^2\,V^{-1}\,s^{-1}}$ as measured by Hall effect. To bring the anticrossing condition close to 90° we had to lower the index of refraction by 0.5% compared to our original calculations when we designed the structure. This inaccuracy on the index of refraction can be related to the uncertainty of the Al content as measured by x-ray diffraction (± 0.01), in combination with the inaccuracy of the model when calculating the index of refraction.[18] Similarly, to bring the theoretical anticrossing at around 90° and 78° for the structures NT3555 and NT3556-3557 it was necessary to lower the barrier index by 0.5%. These observations suggest that the model used for the index of refraction of the barrier is not exact. For instance, the temperature

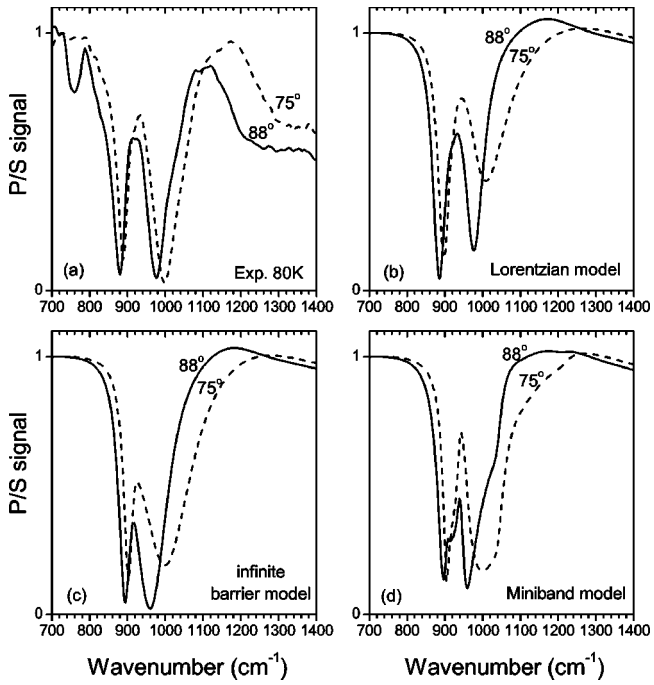

FIG. 5. Panel (a): P/S ratios of wafer NT3429 for 75° and 88° incidence on the cleaved facet. Panels (b)–(d): Simulations of P/S ratios using different dielectric functions for the quantum wells. Panel (b): Lorentzian model with unity oscillator strength. Panel (c): Bound-to-quasibound and bound-to-extended transitions assuming infinite wide barriers. Panel (d) same as (c) with interwell coupling included.

dependence of the high-frequency dielectric constant ε_∞ in AlGaAs alloys is not very well known. With the correction on the index of the barrier we get a reasonable fit of the peak positions.[19] The Lorentzian model also predicts the small dip and shoulder at 920 $\mathrm{cm^{-1}}$. The simulations performed with the parameters of samples NT3555, 3556, and 3557 underestimate the minimum Rabi splitting by about 20 $\mathrm{cm^{-1}}$.

Examples of theoretical reflectivity spectra with the Lorentzian model are shown in Fig. 5(b). They can be compared with the experimental curves in Fig. 5(a). In Fig. 5(a) one can appreciate the decrease of the FWHM of the lower branch when the waveguide resonance is positively detuned with respect to the electronic resonance (75°). As expected, the simulation in Fig. 5(b) indicates that the upper branch should get stronger as the waveguide mode approaches the anticrossing condition. Indeed, the branch closer to the intersubband resonance is the strongest and therefore a transfer of oscillator strength between the two branches occurs in the anticrossing region. Experimentally, in all the studied samples, both branches are equally strong in depth and the waveguide-related peaks are more intense than expected. This latter observation is probably suggesting that the optical indices used in the simulations underestimate the losses that are not related with the intersubband absorption (losses by the gold mirror, free-carrier absorption in the contacting layers, for instance).

Even though not very clear in Fig. 5(b) the Lorentzian model also predicts a small dip or a shoulder at 920 $\mathrm{cm^{-1}}$. This feature was not observed with the cavity-excitonic po-

laritons where the Q factor is very high. This trace of intersubband transition between the polariton branches comes from the high peak absorption in the MQW region in combination with the low Q factor of the cavity. To qualitatively illustrate this assertion, we simplified the calculation by removing the gold mirror to rule out any coupling through some surface plasmon mode, by ignoring the imaginary part of the index of refraction of the contact layer and by using an isotropic dielectric function of the QW's (like in Ref. 10). With this latter simplification we neglect the complex refraction of light inside the QW's. Without the gold mirror, we had to increase the number of wells to 200 to bring the empty cavity resonance at 920 cm^{-1} for an incidence $\theta_0 = 90°$. The FWHM of the intersubband resonance was changed from 58 cm^{-1} to the extreme case of 8 cm^{-1}. We artificially turned ''on'' and ''off'' the imaginary part of the intersubband index of refraction of the QW's. Turning ''off'' the intersubband imaginary index means that we look at the new resonant frequencies of the cavity which is perturbed by the intersubband dispersion. To show these waveguide resonances when the intersubband imaginary index is turned ''off,'' we artificially applied a small power dissipation factor of 0.01 in the MQW. Turning ''on'' means we look at how the absorption affects these resonances. Also, we calculated the average index of refraction in the MQW region. The effective-medium approach was used. The results of this simplified simulation are summarized in Fig. 6. From this figure, qualitative explanations of the central dip can be given.

Due to the Lorentzian derivative shape of the intersubband dispersion [Fig. 6(a)], the waveguide resonance condition is satisfied three times and three dips appear in the reflection spectra [Fig. 6(b)]. At these waveguide resonances, the power enhancement factor (PEF), defined as the ratio between the power density in the MQW and the incident power density in the substrate, is about 23. Basically, Fig. 6(b) illustrates the PEF in the MQW in the absence of intersubband absorption. The positions of the upper (UP) and lower branches (LP) of the polaritons depend weakly on the broadening since the Rabi energy depends mainly on the intersubband dipole moment. As the homogeneous broadening of the transition is reduced, the anomalous dispersion is stronger and therefore the central resonance gets sharper and is always fixed at 920 cm^{-1} independent of the angle of incidence.

For small intersubband broadening, just away from the sharp central resonance in Fig. 6(b), the reflectivity is close to unity and the field leaks weakly inside in the MQW region. The PEF is small, below unity, and is weakly phase dependent. The penetration of the field inside the MQW depends on the reflectivity of the bottom mirror and the relative indices between the substrate and the MQW. Figure 6(c) represents the intersubband loss $\alpha_{ISB} d_{MQW}$ where α_{ISB} is the intersubband absorption coefficient and d_{MQW} the thickness of the MQW. When the intersubband absorption is turned on, the central resonance is quickly damped by the resonant strong absorption. Outside of it, where the reflectivity is close to unity in Fig. 6(b) the wave leaking in the MQW probes the intersubband absorption; in other words attenuated total internal reflection occurs. This is why we experimentally observe small dips and shoulders at the intersubband resonant frequency (Figs. 2 and 3). If the bottom layer were thicker, i.e., if the Q factor of the optical resonator were higher, the power density in the MQW region would be smaller and the central intersubband resonance would be reduced. One can interpret the central dip more rigourously with the help of Ref. 20. When the absorption is very high, the PEF is small (the resonance is strongly damped) and is weakly phase dependent, therefore the total absorption follows a Lorentzian shape.

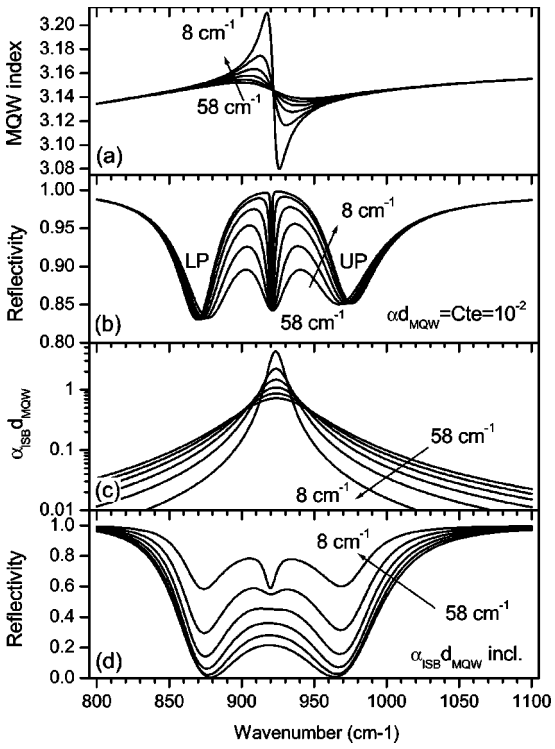

FIG. 6. Simplified calculation for $\theta_0 = 90°$ (no angle averaging). Panel (a): Average index of refraction (real part) in the MQW for a 90° incidence on the cleaved facet. Different full width at half maximum are considered for the intersubband resonance: 58, 48, 38, 28, 18, and 8 cm^{-1}. Panel (b): Reflectivity of P-polarized light by artificially turning off the intersubband imaginary index of refraction. A small constant dissipation factor of 1% was introduced in this calculation. Panel (c): intersubband absorption loss in the MQW, i.e., the product between the absorption coefficient in the MQW and its thickness. Panel (d): same as (b) without the 1% loss and with the QW intersubband absorption turned on.

For large intersubband broadening the central resonance dip in Fig. 6(b) has a similar width to the upper and lower branches. Again, the concept of PEF is useful. The intersubband losses are rather small for such large broadening [Fig. 6(c)], therefore the PEF is still high at resonance and is strongly phase dependent. Away from the 920-cm^{-1} resonance, the intersubband loss gets even smaller which in turn, increases the PEF. The two effects compensate each other, i.e., the total absorption efficiency is constant around 920 cm^{-1}. The dip in Fig. 6(b) disappears in Fig. 6(d), it gets ''blurred'' when the intersubband absorption is turned on.

At the UP and LP polariton frequencies the intersubband

absorption is small for any value of the broadening and therefore the PEF stays high. As far as the intersubband loss $\alpha_{ISB}d_{MQW}$ is below $-1/2\ln R1$, $R1$ being the reflectivity of the bottom contact (inset of Fig. 1), the total absorption will increase with the intersubband loss.[20] Above $-1/2\ln R1$ for the intersubband loss, the polariton resonance will suffer from absorption damping.

Choosing an oscillator strength of unity was a simple approximation since, in principle, some oscillator strength is distributed among the extended states above the barrier. We are conscious that spreading the oscillator strength at higher energy will tend to decrease the minimum Rabi splitting; on the other hand the transitions at higher energy might maintain the strength of the upper branch polariton. Very likely, the fit will not improve by including the bound-to-continuum transitions in the model but we still tried. We calculated the QW absorption coefficient including the bound-to-continuum transitions. Two cases were considered by turning on and off the coupling with the adjacent wells. Coupling on means we take into account the minibands in the vicinity and above of the barrier; coupling off is the same as considering infinitely wide barriers. We used a one-band model to calculate the energy levels and the matrix elements.[21] A Kramers-Kronig transformation was used to derive the real part of the intersubband susceptibility. All simulated spectra are convolved by the Gaussian distribution of angles of incidence, and finally, the P/S ratios are normalized to unity at 700 cm^{-1}. Figures 5(c) and (d) show examples of theoretical P/S spectra with these two models. As expected, in both cases, the minimum Rabi splitting is smaller than that derived with the Lorentzian model and the strength of the upper branch of the polariton versus the angle of incidence is more constant. Overall, the shapes of these curves are far from the experimental curves. The three models considered here fail to give good fits of the experimental curves. Among the three, the Lorentzian model seems to give a better fit. Experimental data show more intense and clear Rabi doublets than the simulations. We speculate about the possibility of having quantum interference effects similar to Fano resonance due to the proximity of the continuum states.[22–24] The measurement probes the reflection of the QWIP structure, not the absorption in the wells. Because the cladding layers contribute to the waveguide loss, calculations are necessary to assess the absorption taking place in the MQW. The result of the calculation for a 80° incidence on the facet is displayed in Fig. 7. Again, three models for the QW dielectric function are considered. The absorption efficiency is predicted to be very strong, which was experimentally confirmed by the strength of the negative peaks of the reflection spectra (Fig. 2). The QW absorption is very strong at the lower and upper branches, even though only the absorption tail of the intersubband resonance is involved at such large detuning from the 920-cm^{-1} electronic resonance.

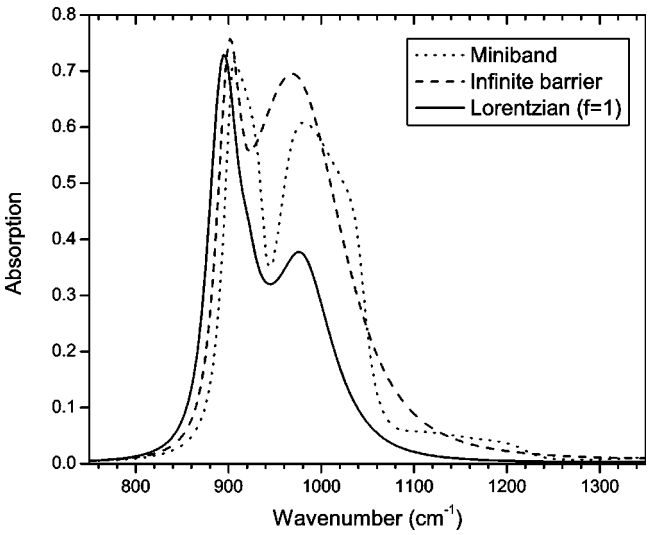

FIG. 7. Theoretical absorption efficiency for *P*-polarized light incidence at 80° on the cleaved facet. The results for the three models of QW dielectric functions are compared.

IV. ELECTRICAL MEASUREMENTS

The first objective of this study was to observe the vacuum-field Rabi splitting; another objective was to investigate the performance of such a structure when operated as an infrared photodetector. We first measured the photocurrent spectra with incident light at Brewster angle on the plane of the layers (see inset in Fig. 8). Doing so, we probe the excited states and avoid the interference of the waveguide structure. Figure 8 is a contour plot where normalized spectra are displayed for different applied voltages. At 3 and 7 V we observed an anticrossing of the states in the vicinity of the barrier at 900–950 cm^{-1}. At these particular voltages, the positions of minibands above the barrier (right panel of Fig. 8) are strongly modified. At vanishing bias we identify three minibands (MB1-3) above the barrier; in photocurrent spectroscopy they appear at 1023, 1170, and 1400 cm^{-1}. These positions are an excellent match to the theoretical absorption spectrum calculated for 0 V.[25] The theoretical prod-

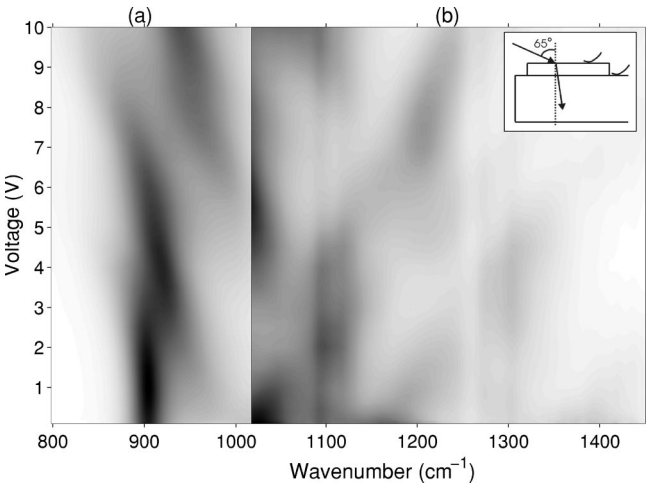

FIG. 8. Contour plot of photocurrent spectra versus applied bias at 80 K. The infrared light is close to Brewster incidence (65°) on the plane of the layers of NT3429. The left panel (a) shows the long-wavelength side (below 1020 cm^{-1}). To show the bound-to-extended transitions the gray scale was expanded in the right panel (b). All spectra have been normalized by their area.

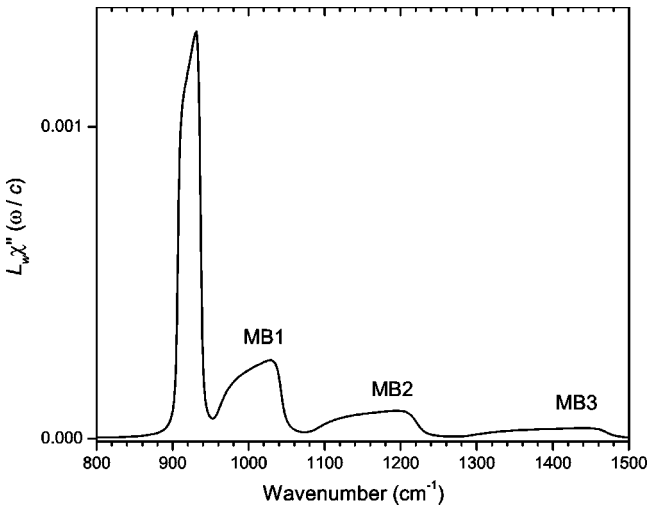

FIG. 9. Theoretical absorption of one quantum well at 0 V, including interwell coupling (Bloch waves).

uct $L_w\chi''\omega/c$, where ω is the light frequency, c the light velocity, L_w the width of the QW, and χ'' the imaginary part of the intersubband susceptibility is plotted in Fig. 9. This figure shows the predicted energies of the bound-to-miniband transitions. The anticrossing observed at 3(7) V corresponds to the situation where MB1(2) is brought in resonance with the first excited state of the upstream adjacent quantum well. The occurrence of the bound-to-miniband transition suggests that the coherence length of electrons extends over several periods. It also proves that some oscillator strength is distributed within the extended states. Therefore it is still unclear why the Lorentzian model with maximum oscillator strength produces a better fit to the observed Rabi splitting.

The photocurrent was then measured with an incident angle of 80° on the cleaved facet. Two types of devices were tested: devices with a gold mirror covering the top of the mesas, and devices with a narrow top ring contact, i.e., with a large area of GaAs/air interface. The first type of device uses the waveguide, whereas the other type cannot hold very confined waveguide modes. Spectra at 1 and 4 V are displayed in Figs. 10(a) and (b). Below 1080 cm^{-1} the devices with the waveguide show stronger absorption than those with the GaAs/air interface. The devices with the GaAs/air interface have stronger absorption at 1200 cm^{-1} due to the excitation of a weakly confined waveguide mode. Close to the intersubband resonance (900–920 cm^{-1}) the GaAs/air devices exhibit a strong signal because the light leaks significantly into the MQW. The ratio of photocurrent spectra between the two types of devices reveal the absorption enhancement by the waveguide. This is shown in Fig. 10(c) where we can identify two peaks at 870 and 990 cm^{-1}. These positions can be compared with the negative peaks of the reflection measurement (spectrum at 80° in Fig. 2) at 884 and 988 cm^{-1}. The maximum at 870 cm^{-1} in the ratio of photocurrents does not exactly match the position of the reflection minimum (884 cm^{-1}) because the photocurrent with the GaAs/air interface is rapidly varying in this spectral range. The ratio of photocurrents between devices with

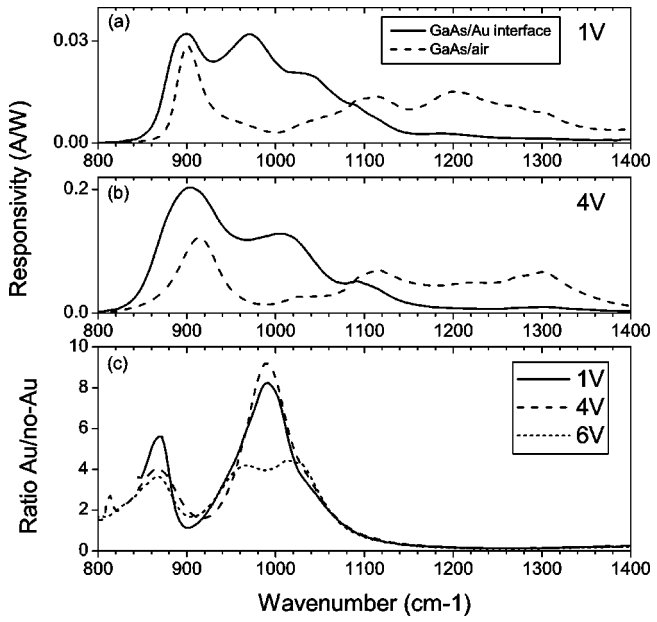

FIG. 10. Panels (a) and (b): comparison of the 80-K responsivity spectra at 1 and 4 V between devices with a top GaAs/Au interface and devices with a dielectric GaAs/air interface. The light is directed at 80° onto the cleaved facet. Panel (c) shows the ratio of these spectra at 1, 4, and 6 V. At 6 V, the Rabi splitting is significantly modified.

GaAs/Au and GaAs/air interfaces is not constant with voltage. For instance at 6 V, close to the anticrossing of states at the barrier edge, the dielectric function of the well ε_{zz}, is so much perturbed that the vacuum-field Rabi features are significantly changed [Fig. 10(c)]. An infrared modulator based on the vacuum-field Rabi splitting sensitivity with ε_{zz} could be designed with asymmetric or double quantum wells.

The dark current of the device was measured at different

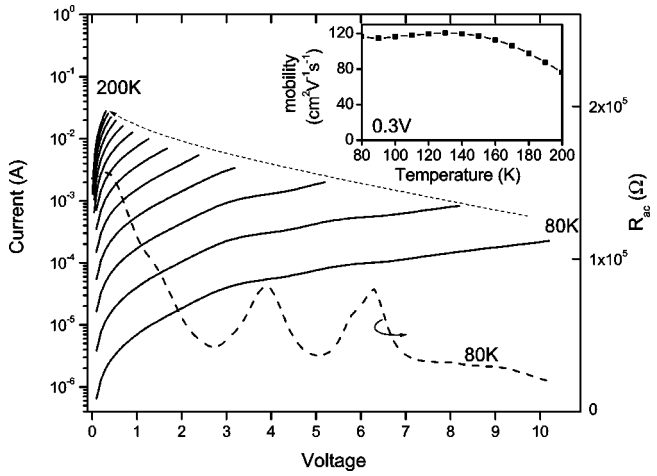

FIG. 11. Leakage current at different temperatures of 1-mm^2 large device from the wafer NT3429. The temperature step is 10 K. The dashed line represents the differential resistance at 80 K. The peaks at 3.9 and 6.3 V show the perturbation of the conduction states in the vicinity of the barrier edge. The inset is the derived electron mobility versus temperature at 0.3 V.

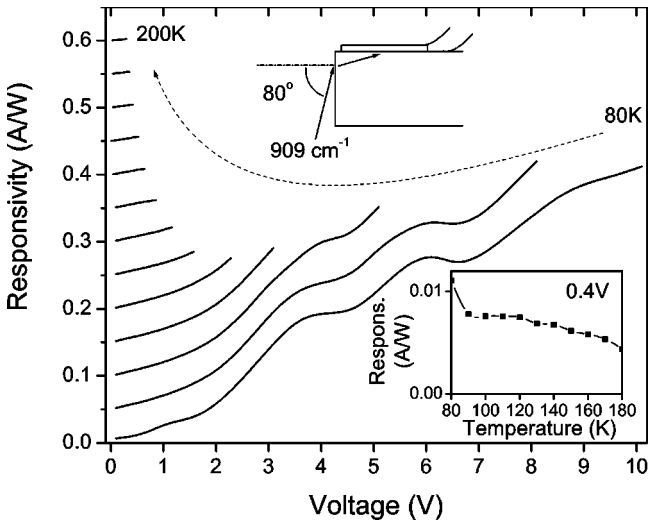

FIG. 12. Responsivity of NT3429 at 909 cm^{-1} for different temperatures. The temperature step is 10 K. The responsivity is given for *P*-polarized light directed at 80° incidence onto the facet. For clarity, the curves are shifted relative to each other by 0.05 A/W. The inset plot shows the responsivity at 0.4 V versus temperature.

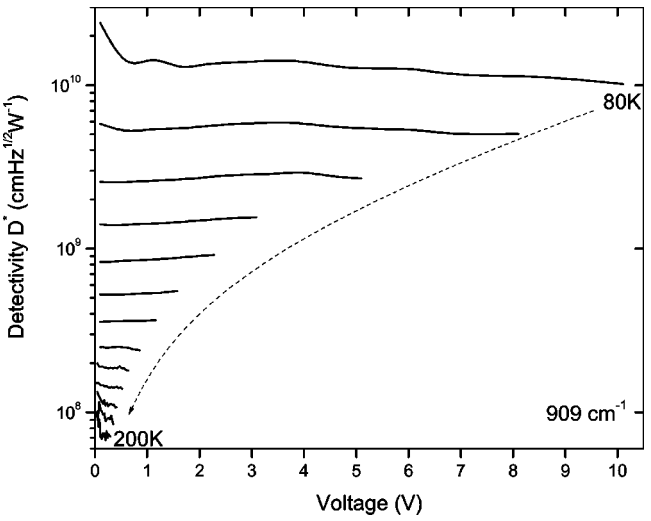

FIG. 13. Derived detectivity of NT3429 at 909 cm^{-1} for different temperatures. The temperature step is 10 K. The detectivity is given for *P*-polarized light directed at 80° incidence onto the facet.

temperatures. Figure 11 shows the current-voltage characteristics for a 1-mm^2 device from 80 to 200 K. At low temperatures, we see a strong modulation of the differential resistance R_{ac}. Local maxima of R_{ac} are found at 3.9 and 6.3 V, i.e., exactly in the range of voltages where anticrossing of states were observed close to the barrier edge. From this set of curves we derive an activation energy of 104 meV, or equivalently 840 cm^{-1}. The Fermi energy is only 0.7 meV (6 cm^{-1}) in the well. This value of activation energy is reasonably close to the cutoff wavelength of the photocurrent measured at low voltage (875 cm^{-1}), minus the Fermi energy. The mobility is then derived, and the inset of Fig. 11 shows the mobility at 0.3 V versus temperature. Surprisingly, its value is lower than expected. This is probably due to the band bending caused by the modulation doping. Phonon interaction starts to be the main scattering mechanism above 150 K.

The infrared response of a device with a GaAs/Au interface was measured by focusing, at 80° incidence, a lead-salt laser diode beam onto the cleaved facet. Only 6 mW was directed onto the facet. The laser diode wavenumber was tuned by temperature at 909 cm^{-1}, and final calibration was performed with a calibrated 1000-K blackbody source. The results are plotted in Fig. 12 for different temperatures. Close to 4 and 6 V, we find the same features as in the dark current due to the anticrossing of the states. With temperature, we saw small variations of the photocurrent. The decrease of response with temperature (see the inset of Fig. 12) is slightly faster than that of mobility due to the redshift of absorption with temperature. From these measurements of activation energy, mobility, and responsivity we find the devices behave consistently. The detectivity of the device D^* was derived according to the equation

$$D^* = \frac{R}{\sqrt{4qgJ}}, \tag{2}$$

where R is the responsivity, q the electronic charge, g the noise gain which was assumed to be close to the photoconductive gain, J the current density flowing in the device. From the reflection R_p measurements (Fig. 2) we derive an absorption quantum efficiency $\eta = 1 - R_p \approx 0.4$ at 909 cm^{-1}, a value which is used for the calculation of g. The detectivity for different temperatures is shown in Fig. 13. The detectivity is high at low temperature and degrades by two orders of magnitude from 80 to 200 K.

The behavior of highly doped samples with comparable cutoff wavelength and activation energy was found to be different.[26] At 80 K, highly doped samples show a detectivity one order of magnitude smaller than our structure due to their higher leakage current. However, at 200 K, the detectivity of NT3429 and that reported in Ref. 26 are both similar. Looking into details at the data of the 10^{12}-cm^{-2} doped structure of Ref. 26, we found that at 1 V, and between 80 and 200 K, the dark current increases by a factor of $\sim 3 \times 10^4$, and the responsivity by a factor of 17. The increase of responsivity, first attributed to the temperature dependence of the mobility, is actually not detected in the dark current. The reason for this phenomenon is not clear yet and will be the subject of future studies. In highly doped samples, the increase of responsivity with temperature compensates for the high current to the point that, highly doped QWIP's and NT3429 have the same detectivity at 200 K.

V. CONCLUSION

We have demonstrated, both optically and electrically, the vacuum-field Rabi splitting due to bound-to-quasibound intersubband transitions in quantum-well infrared photodetectors. The initial objective of this study was to show high absorption efficiencies in low-doped structures at grazing in-

ternal incidence. We find it is essential to take into account the possible occurrence of the vacuum-field Rabi splitting. The exact fitting of the Rabi-splitted reflection spectra does not seem obvious. The structure studied here involved bound-to-quasibound and bound-to-continuum Bloch wave intersubband transitions. The continuum states add complexity to the analysis of the vacuum-field Rabi splitting. This suggests studying the evolution of the Rabi splitting from bound-to-bound, bound-to-quasibound to bound-to-free intersubband transitions.

ACKNOWLEDGMENT

We are grateful to M. Załużny for useful discussions. The authors would like to thank DRDC-Valcartier who partly supported this work.

*Electronic address: emmanuel.dupont@nrc-cnrc.gc.ca

[1] A. Bonvalet, J. Nagle, V. Berger, A. Migus, J.-L. Martin, and M. Joffre, Phys. Rev. Lett. **76**, 4392 (1996).

[2] R.A. Kaindl, S. Lutgen, M. Woerner, T. Elsaesser, B. Nottelmann, V.M. Axt, T. Kuhn, A. Hase, and H. Künzel, Phys. Rev. Lett. **80**, 3575 (1998).

[3] F. Eickemeyer, M. Woermer, A.M. Weiner, T. Elsaesser, R. Hey, and K.H. Ploog, Appl. Phys. Lett. **79**, 165 (2001).

[4] K. Reimann, C. W. Luo, M. Woerner, T. Elsaesser, R. Hey, and K.H. Ploog, *7th International Conference on Intersubband Transitions in Quantum Wells (ITQW'03)*, Evolène (Switzerland), Sept. 2003, paper I56.

[5] C. Weisbuch, M. Nishioka, A. Ishikawa, and Y. Arakawa, Phys. Rev. Lett. **69**, 3314 (1992).

[6] P.G. Savvidis, J.J. Baumberg, R.M. Stevenson, M.S. Skolnick, D.M. Whittaker, and J.S. Roberts, Phys. Rev. Lett. **84**, 1547 (2000).

[7] M. Saba, C. Ciuti, J. Bloch, V. Thierry-Mieg, R. Andr, L.S. Dang, S. Kundermann, A. Mura, G. Bonglovanni, J. Staehli *et al.*, Nature (London) **414**, 731 (2001).

[8] P.G. Lagoudakis, M.D. Martin, J.J. Baumberg, A. Qarry, E. Cohen, and L.N. Pfeiffer, Phys. Rev. Lett. **90**, 206401 (2003).

[9] A. Liu, Phys. Rev. B **55**, 7101 (1997).

[10] D. Dini, R. Köhler, A. Tredicucci, G. Biasiol, and L. Sorba, Phys. Rev. Lett. **90**, 116401 (2003).

[11] E. Dupont, M. Gao, H.C. Liu, Z.R. Wasilewski, A. Shen, M. Załużny, S.R. Schmidt, and A. Seilmeier, Phys. Rev. B **61**, 13 050 (2000).

[12] E. Dupont, H.C. Liu, S.R. Schmidt, and A. Seilmeier, Appl. Phys. Lett. **79**, 4295 (2001).

[13] H. Sakaki, T. Noda, K. Hirakawa, M. Tanaka, and T. Matsusue, Appl. Phys. Lett. **51**, 1934 (1987).

[14] K.L. Campman, H. Schmidt, A. Imamoglu, and A.C. Gossard, Appl. Phys. Lett. **69**, 2554 (1996).

[15] Y. Zhu, D.J. Gauthier, S.E. Morin, Q. Wu, H.J. Carmichael, and T.W. Mossberg, Phys. Rev. Lett. **64**, 2499 (1990).

[16] In this paper the oscillator strength is taken to its simplest form: $2m^{\star}\omega_0 d^2/\hbar$ where ω_0 is the light frequency, d the dipole matrix element between the states, $m^{\star}$ the effective mass in the well. A more rigorous definition of the oscillator strength is given by C. Sirtori *et al.*, Phys. Rev. B **50**, 8663 (1994). Using this more rigorous technique for the calculation of the oscillator strength would lead to slightly smaller Rabi splitting.

[17] M. Załużny and C. Nalewajko, Phys. Rev. B **59**, 13 043 (1999).

[18] O.K. Kim and W.G. Spitzer, J. Appl. Phys. **50**, 4362 (1979).

[19] In the calculations, at 920 cm^{-1} and 80 K, the real part of the index of refraction of undoped GaAs, $Al_{0.197}Ga_{0.803}As$ barrier, and GaAs contact were, respectively, 3.2356, 3.1279, and 2.7045.

[20] M.S. Ünlü and S. Strite, J. Appl. Phys. **78**, 607 (1995).

[21] In the calculation, the Al content in the barrier was set to 0.197, the barrier height $\Delta E_c = 168$ meV. The band bending due to the modulation doping was included but not the nonparabolicity.

[22] H. Schmidt, K.L. Campman, A.C. Gossard, and A. Imamoğlu, Appl. Phys. Lett. **70**, 3455 (1997).

[23] J. Faist, F. Capasso, C. Sirtori, A. Hutchinson, K.W. West, and L.N. Pfeiffer, Appl. Phys. Lett. **71**, 3477 (1997).

[24] W. Pötz, Superlattices Microstruct. **26**, 141 (1999).

[25] Y. Fu, Superlattices Microstruct. **30**, 69 (1999).

[26] H.C. Liu, R. Dudek, A. Shen, E. Dupont, C.Y. Song, Z.R. Wasilewski, and M. Buchanan, Appl. Phys. Lett. **79**, 4237 (2001), and for more details, see H.C. Liu, R. Dudek, A. Shen, E. Dupont, C.Y. Song, Z.R. Wasilewski, and M. Buchanan, Int. J. High Speed Electron. Syst. **12**, 803 (2003).